Transient birefringence and dichroism in ZnO studied with fs-time-resolved spectroscopic ellipsometry

O. Herrfurth [1,*] S. Richter [2,3] M. Rebarz [3] S. Espinoza [3] J. Zúñiga-Pérez [4] C. Deparis,[4] J. Leveillee,[5] A. Schleife [6,†]
M. Grundmann [1] J. Andreasson [3] and R. Schmidt-Grund [7]

[1]*Universität Leipzig, Felix-Bloch-Institut für Festkörperphysik, Linnéstraße 5, 04103 Leipzig, Germany*
[2]*Linköpings universitet, Institutionen för fysik, kemi och biologi, 58183 Linköping, Sweden*
[3]*ELI Beamlines/Fyzikální ústav AV ČR, v.v.i., Za Radnicí 835, Dolní Břežany, Czech Republic*
[4]*Université Côte d'Azur, CRHEA-CNRS, rue Bernard Grégory, Valbonne, France*
[5]*The University of Texas at Austin, Oden Institute for Computational Engineering and Sciences,*
201 E. 24th Street, P.O. Box 4.102, Austin, Texas IL 78712-1229, USA
[6]*University of Illinois at Urbana-Champaign, Dep. of Materials Science and Engineering,*
1304 W. Green St., Urbana, IL 61801, USA
[7]*Institut für Physik, Technische Universität Ilmenau, Weimarer Straße 25, 98693 Ilmenau, Germany*

The full transient dielectric-function (DF) tensor of ZnO after UV-laser excitation in the spectral range 1.4–3.6 eV is obtained by measuring an *m*-plane-oriented ZnO thin film with femtosecond (fs)-time-resolved spectroscopic ellipsometry. From the merits of the method, we can distinguish between changes in the real and the imaginary part of the DF as well as changes in birefringence and dichroism, respectively. We find pump-induced switching from positive to negative birefringence in almost the entire measured spectral range for about 1 ps. Simultaneously, weak dichroism in the spectral range below 3.0 eV hints at contributions of inter-valence-band transitions. Line-shape analysis of the DF above the band gap based on discrete exciton, exciton-continuum, and exciton-phonon-complex contributions shows a maximal dynamic increase in the transient exciton energy by 80 meV. The absorption coefficient below the band gap reveals an exponential line shape attributed to Urbach-rule absorption mediated by exciton–longitudinal-optic-phonon interaction. The transient DF is supported by first-principles calculations for 10^{20} cm^{-3} excited electron-hole pairs in ideal bulk ZnO.

I. INTRODUCTION

Transient optical properties [1,2] represented by the dielectric function (DF) following ultrafast laser excitation can be obtained using time-resolved spectroscopic ellipsometry (tSE) [3,4]. In contrast to conventional pump-probe experiments that do not investigate the change in light polarization upon reflection (transmission), spectroscopic ellipsometry measures simultaneously relative amplitude *and* phase information of the reflected (transmitted) electromagnetic fields [5]. This allows a clear distinction between changes in extinction coefficient and refractive index. Polarization- and direction-dependent (anisotropic) optical properties are described by a DF tensor with at least two different tensor components [6]. In the regime of linear optics, the literature on transient optical

anisotropy at the femtosecond time scale is mostly focused on circular dichroism [7–13]. Transient linear dichroism was obtained from single-wavelength stimulated Raman-scattering measurements [14,15]. Transient off-diagonal DF tensor elements can be obtained from magneto-optical Kerr-effect measurements [16]. All these effects of transient optical anisotropy can be studied individually, but they are subsumed in the underlying material properties, which means in general the transient DF. Although some of the mentioned setups seem to be capable of providing the data necessary for obtaining the full DF tensor, this has not been demonstrated.

In this paper, we report the full transient DF tensor of ZnO in the spectral range 1.4–3.6 eV obtained by tSE. We choose the prototypical wide-band-gap semiconductor ZnO [17,18] for this study because its wurtzite crystal structure leads to the simplest form of optical anisotropy—namely, birefringence and dichroism [6]. In addition, the strong carrier–longitudinal optic (LO)-phonon interaction in ZnO has a significant effect on the optical properties of ZnO [19,20]. Hence the transient DF might hint on anisotropic carrier-phonon interaction upon laser excitation. Earlier time-resolved spectroscopy studies on ZnO in the reflection [3,21–24] or transmission [21,25–27] configuration mostly neglected its anisotropic optical properties.

---

*oliver.herrfurth@physik.uni-leipzig.de
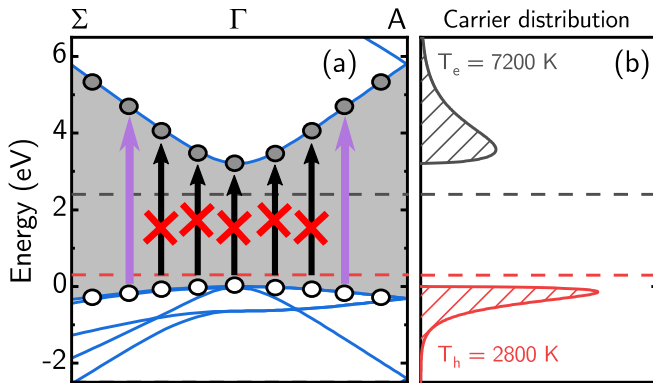†schleife@illinois.edu

FIG. 1. (a) Sketch of the Brillouin zone of ZnO near the Γ point indicating relevant optical transitions along with the carrier distribution after thermalization (a few hundred femtoseconds). The pump transitions are indicated by violet arrows. Carrier-carrier scattering results in broad Fermi-Dirac distributions of electrons (filled circles) in the conduction band and holes (open circles) in the valence bands. (b) These hot carriers feature effective temperatures of several thousand kelvins, which results in their quasi Fermi level (chemical potential, dashed lines) being shifted into the band gap. Band-to-band transitions indicated by black arrows are partially blocked. (Adapted from Ref. [3].)

II. EXPERIMENT

The pump-probe-based tSE setup [28] is driven by a kilohertz-repetition-rate Ti:sapphire laser (35 fs FWHM pulse duration) that generates UV-pump and white-light probe pulses. Polarization-resolved reflectance-difference spectra are acquired in polarizer-sample-compensator-analyzer configuration by scanning an optical delay line up to 5 ns at various compensator azimuth angles. The ellipsometric spectra (isotropic Mueller matrix elements N, C, and S [5]) at a given time delay Δt are reconstructed from the reflectance-difference spectra after noise reduction [29] and chirp correction (Appendix A). The spectral and temporal bandwidths amount to 5 nm in the near-UV and about 100 fs, respectively. The angle of incidence is 60° for the probe beam and 54° for the pump beam, respectively. A sketch of the setup is provided in Ref. [28]. All experiments were conducted at room temperature.

We investigate an *m*-plane-oriented ZnO thin film of 38 nm thickness (1 nm surface roughness) grown by molecular-beam epitaxy (MBE) on an *m*-plane sapphire substrate [30]. X-ray diffraction measurements confirm the single-crystal nature of the thin film and its precise crystallographic orientation. The structural characterization of the sample is detailed in Appendix B. The material's optic axis is oriented parallel to the sample surface. The sample is thin enough to assume approximately homogeneous excitation by a nonresonant 4.67-eV (266 nm, polarization horizontal to the plane of incidence) pump pulse with 50 nm penetration depth [31]. The substrate is transparent for the pump light. The pump fluence at the sample amounts to 720 μJ/cm^2 such that the estimated density of excited electron-hole pairs is 3×10^{20} cm^{-3}. We sketch the relevant electronic transitions for 4.67 eV optical excitation near the Γ point in Fig. 1 along with the carrier distribution after thermalization [3].

III. DATA ANALYSIS

The complex-valued dielectric function ε is typically written as

$$\varepsilon = \varepsilon_1 + i\varepsilon_2 = (n + i\kappa)^2, \qquad (1)$$

where the second equality shows the connection to the complex index of refraction composed of the refractive index n and the extinction coefficient κ [6,32]. The absorption coefficient is then $\alpha = 4\pi\kappa E/hc$ (with photon energy E, Planck's constant h, and speed of light c). In the case of ZnO [17], the wurtzite crystal structure entails a DF tensor of the form

$$\varepsilon = \begin{pmatrix} \varepsilon^{sc} & 0 & 0 \\ 0 & \varepsilon^{sc} & 0 \\ 0 & 0 & \varepsilon^{pc} \end{pmatrix}, \qquad (2)$$

with the DF tensor components for polarization perpendicular (ε^{sc}) and parallel (ε^{pc}) to the optic axis [insets in Figs. 2(a) and 2(b)]. Therefore two spectroscopic ellipsometry measurements with perpendicular and parallel orientation of the optic axis to the plane of incidence at the same spot on the sample are combined to obtain the full DF tensor. The simultaneous treatment of multiple measurements poses no source of error in the data analysis, if (1) the sample is not modified over the duration of the measurements and (2) equal excitation conditions are provided for the individual measurements. In our experiment, condition (1) is fulfilled because the pump fluence is well below the ablation threshold of ZnO (a few J/cm^2) [33–35]. Condition (2) is also fulfilled because the excited carrier density is almost equal for the two orientations of the sample, which is related to the similar reflectance (2% difference) at the pump photon energy.

The numerical DF tensor components were obtained from a wavelength-by-wavelength analysis of the measured ellipsometric spectra using a transfer-matrix model [36]. Surface roughness was implemented via the Bruggeman effective-medium approach [37], and the substrate DF was taken from a reference measurement. The numerical approach does not require any beforehand assumptions on the line shape of the DF.

IV. TRANSIENT DIELECTRIC-FUNCTION TENSOR

Figures 2(a) and 2(b) feature the spectra of the DF tensor components ε^{sc} and ε^{pc} of the ZnO thin film at selected pump-probe delays Δt directly after pumping (left column, "excitation"). The right column of Fig. 2 ("relaxation") shows the recovery of the DF to its steady-state value starting approximately 1 ps after arrival of the pump pulse. The transient birefringence $n_e - n_o$ and dichroism $\kappa_e - \kappa_o$ spectra [38] shown in Figs. 2(c) and 2(d) are calculated from the DF tensor components [39]. Complex-plane representations (see Appendix E) of the DF tensor components are depicted in Figs. 3(a)–3(d). First-principles DF tensor components are shown as dashed gray lines. See Appendix C for technical details about the first-principles calculations. Transient evaluations are shown in Fig. 4. See the Supplemental Material for surface plots of the transient DF [40].

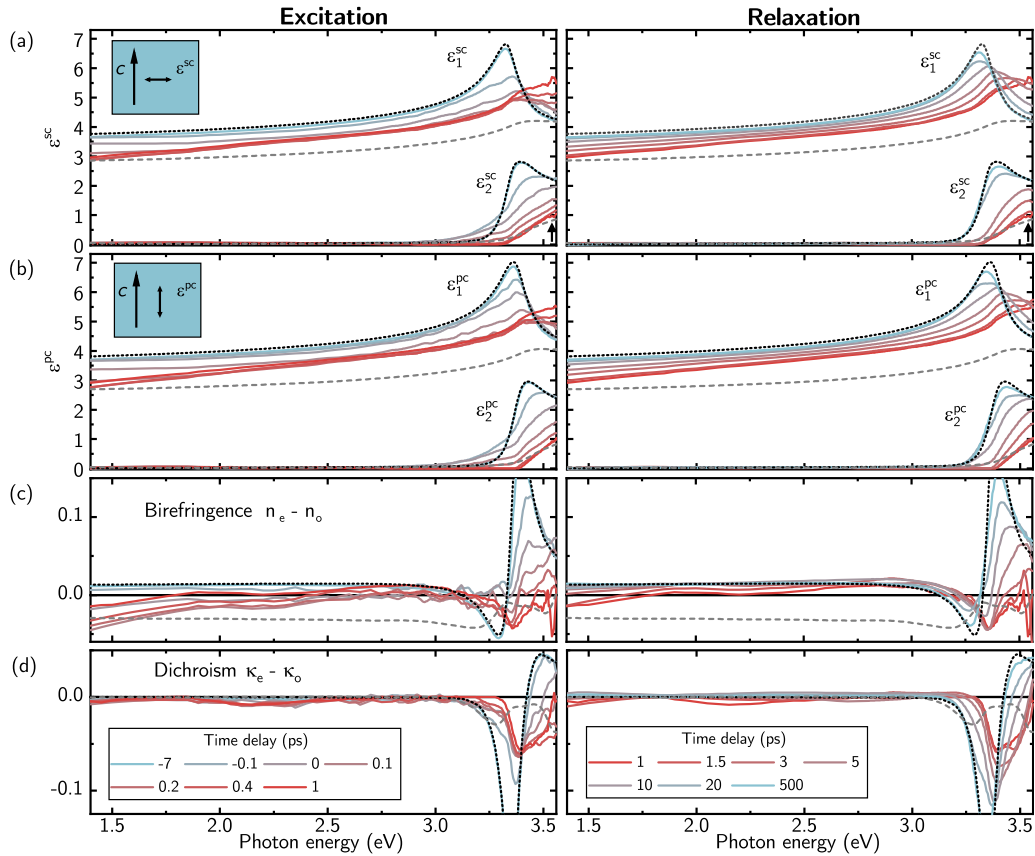At negative Δt [41], the reference DF obtained from a commercial ellipsometer is reproduced (black dotted lines in

FIG. 2. Transient DF tensor components (a) ε_2^{sc} and (b) ε_2^{pc} as well as (c) birefringence and (d) dichroism [38] at selected time delays Δt obtained using wavelength-by-wavelength analysis. The left column comprises time delays around $\Delta t = 0$ (excitation), whereas the right column shows $\Delta t \geqslant 1$ ps (relaxation). The blue rectangles (insets) feature the orientation of the optic axis (single arrow) in the sample in relation to the direction of the DF tensor components (double arrow). The dashed gray lines show the results from first-principles calculations accounting for 10^{20} cm^{-3} excited charge carriers at elevated temperatures [3], and the dotted black lines correspond to the reference spectra obtained with a commercial ellipsometer. The black arrows mark a peak structure in ε_2^{sc} which is observed for $\Delta t = 1$ ps and leads to a characteristic loop in the complex-plane representation (Fig. 3).

Fig. 2). The maximum in ε_2^{sc} (ε_2^{pc}) is associated with excitonic absorption from the light-hole and heavy-hole (split-off) valence bands according to optical selection rules [19]. The spin-orbit splitting amounts to about 36 meV [42], which

determines the difference of the exciton energy of ε_2^{sc} and ε_2^{pc}. The fine structure due to the crystal-field splitting (light and heavy holes) cannot be resolved at room temperature [42]. Thus we model the exciton resonance in ε_2^{sc} by a single
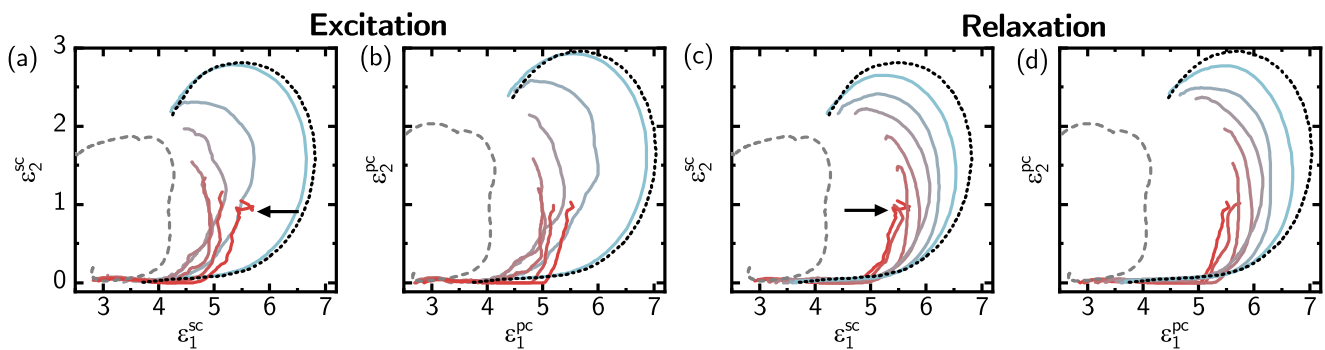

FIG. 3. Complex-plane representation (see Appendix E) of the DF tensor components in Figs. 2(a) and 2(b). The energy increases along the counterclockwise direction of the curve. The dashed gray lines show the results from first-principles calculations accounting for 10^{20} cm^{-3} excited charge carriers at elevated temperatures [3], and the dotted black lines correspond to the reference spectra obtained with a commercial ellipsometer. The black arrows mark a peak structure in ε_2^{sc} which is observed for $\Delta t = 1$ ps and leads to a characteristic loop in the complex-plane representation.
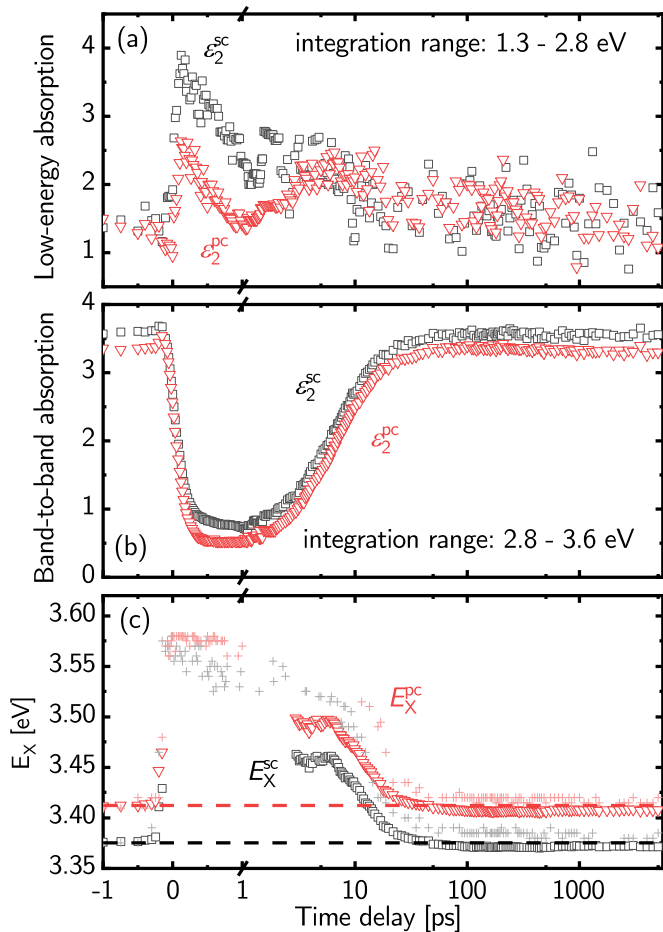
FIG. 4. (a) Integrated value of $\varepsilon_2^{\text{sc}}$ (black) and $\varepsilon_2^{\text{pc}}$ (red) in the spectral range 1.4–2.8 eV in units of meV. Note the horizontal axis break at 1 ps. (b) Integrated value of $\varepsilon_2^{\text{sc}}$ (black) and $\varepsilon_2^{\text{pc}}$ (red) in the spectral range 2.8–3.6 eV in units of meV. (c) Transient exciton energy E_{X} (same color code as in previous panels) as obtained from the line-shape-model equations (3a)–(3c) (squares and triangles) and the read-off peak energy (crosses). The read-off peak energies are rigidly shifted by -20 meV such that they agree with the steady-state values from the oscillator model. The exciton energy cannot be determined from the line-shape analysis when most of the absorption is shifted out of the measured spectral range. The dashed lines indicate the respective steady-state exciton energies.

oscillator (3a). The thin film is transparent for photon energies below 3.2 eV and exhibits positive birefringence in this spectral range. With increasing photon energy, both birefringence and dichroism display a negative-valued minimum followed by a positive-valued maximum, which is an effect of the aforementioned selection rules.

For small positive time delay Δt, the absorption above the band gap represented by ε_2 is strongly damped, accompanied by the simultaneous decrease in ε_1. This is clearly visualized by the shrinking radius of the semicircle of the DF in complex-plane representation [Figs. 3(a) and 3(b)]. At $\Delta t = 0$, the absorption edge is already smeared out and strongly decreased [Figs. 2(a) and 2(b)]. We observe $\varepsilon_2 > 0$ in the spectral range 3.0–3.3 eV. The line shape of the corresponding absorption coefficient (Fig. 6) appears monoexponential, reminiscent of

Urbach-rule absorption [43,44]. Remarkably, the corresponding birefringence [Fig. 2(c)] switches from positive—being the steady state—to negative until $\Delta t \approx 400$ fs, and the local peak structures above 3.2 eV almost disappear completely in both birefringence and dichroism.

In addition, we observe a simultaneous shift of the absorption edge to higher photon energies [Figs. 2(a) and 2(b)]. The largest blueshift is reached after 700 fs when $\varepsilon_2^{\text{sc}}$ ($\varepsilon_2^{\text{pc}}$) has become zero up to 3.33 eV (3.38 eV) and most of the spectral weight of the absorption is shifted out of the measured spectral range also demonstrated by the integrated value of ε_2 in Fig. 4(b) [45]. The exciton peak is not observed anymore at the original peak position; instead a flat edge occurs around 3.6 eV [Figs. 2(a) and 2(b)] which transforms back to a clear peak structure (marked by a black arrow) not until 1 ps has passed. This peak structure produces a loop in the complex-plane representation of the DF [Figs. 3(a) and 3(c)]. For $\varepsilon_2^{\text{pc}}$, we expect a similar peak to occur just above our measured spectral range. Birefringence changes back from negative to positive in the entire spectral range between $\Delta t = 0.2$ and 1 ps [Fig. 2(c)]. Absorption recovery starts from higher energies for $\Delta t > 1$ ps [Figs. 2(a) and 2(b)] concomitantly shifting to lower energies and is not yet fully completed after 5 ns [Fig. 4(c)].

Broad weak absorption channels in the band gap [Figs. 2(a) and 2(b) and Supplemental Material] with indications for a local maximum around 1.7 eV are rapidly induced by the pump laser pulse also seen in the integrated ε_2 [Fig. 4(a)]. The related dichroism [Fig. 2(d)] is small, but a tentative local minimum is located at 2.2 eV at $\Delta t = 1$ ps. The maximal amplitude of the integrated absorption is reached after 100 fs (i.e., instantaneous within the temporal resolution of our experiment) for both tensor components. These broad absorption channels vanish with a characteristic time of 1 ps [Fig. 4(a)] and are not observed anymore after 20 ps.

V. DISCUSSION

For both DF tensor components ε^{sc} and ε^{pc}, transient physical parameters are extracted from a line-shape analysis of the imaginary part of the numerical DF $\varepsilon_2 = \varepsilon_2^{\text{X}} + \varepsilon_2^{\text{cont}} + \varepsilon_2^{\text{EPC}}$ in the spectral range above 3.0 eV. The line shape is based on Elliott's model [46] including a Gaussian broadening parameter γ and extended by exciton-phonon complexes [20,47]:

$$\varepsilon_2^{\text{X}}(E) = \frac{A_{\text{X}}}{E^2} \sum_{n=1}^{3} \left[\frac{1}{\gamma n^3} \exp\left(-\frac{[E - E_{\text{X}}(n)]^2}{\gamma^2} \right) \right], \quad (3a)$$

$$\varepsilon_2^{\text{cont}}(E) = \frac{A_{\text{C}}}{E^2} \frac{1 + \text{erf}\left(\frac{E - E_{\text{G}}}{\gamma}\right)}{1 - \exp(-2\xi)}, \quad (3b)$$

$$\varepsilon_2^{\text{EPC}}(E) = A_{\text{EPC}} \sum_{m=1}^{2} \left[b^{m-1} \varepsilon_2^{\text{X}}(E - mE_{\text{Ph}}) \right]. \quad (3c)$$

Contributions of discrete exciton transitions at energies $E_{\text{X}}(n) = E_{\text{G}} - E_{\text{B}}^{\text{X}}/n^2$ with binding energy E_{B}^{X} and band gap E_{G} are represented by ε_2^{X}. We take $n = 1, 2, 3$ exciton states into account [48]. Exciton-continuum contributions are parametrized by $\varepsilon_2^{\text{cont}}$, where $\xi^2 = \pi^2 |E_{\text{B}}^{\text{X}}/(E - E_{\text{G}})|$. A_{X}
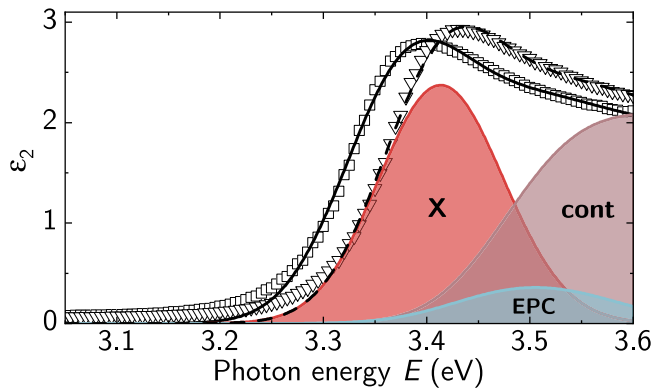
FIG. 5. Line-shape analysis of the steady-state spectra for $\Delta t < 0$ (black lines) of the wavelength-by-wavelength DF of ε_2^{sc} (squares) and ε_2^{pc} (triangles) using the oscillator-model functions (colored areas) given in Eqs. (3a)–(3c). The oscillator-model functions are shown here for ε_2^{pc} only.

and A_C are amplitude parameters proportional to the corresponding transition matrix elements [19]. Exciton-phonon complexes (EPCs) [19,49] are modeled via ε_2^{EPC}, where E_{Ph} is an effective energy of the phonon cloud constituting the EPC. A_{EPC} is the overall amplitude factor, and b is the amplitude ratio of the $(m + 1)$st to the mth phonon replica such that $F_{EPC} = A_{EPC} \sum_m b^{m-1}$ expresses the ratio of the EPC to the discrete exciton contribution [49]. The parameters γ, E_B^X, A_{EPC}, and b are assumed to be identical for both DF tensor components ε_2^{sc} and ε_2^{pc} to discard correlations. Furthermore, a constant offset of 36 meV between the band-gap parameters E_X^{sc} and E_X^{pc} is assumed [42], which means that we neglect a shift between the topmost and the split-off valence band. The EPC peaks are not clearly observed in the spectra [Figs. 2(a) and 2(b)], but their contribution is still necessary for a physically meaningful line-shape fit [20,49]. Therefore we approximate $E_{ph} = 50$ meV in the line-shape analysis in accordance with the literature [3,20,49]. Due to these assumptions, we cannot directly deduce information on the transient electron-phonon interaction from the line shape of the EPC.

Line-shape-model spectra for the steady-state DF are shown in Fig. 5. The colored areas correspond to the contributions of discrete excitons and exciton-phonon complexes as well as exciton-continuum contributions. Model parameters for the steady-state spectra are tabulated in Table I. The steady-state exciton energy E_X is about 60 meV larger than the literature value [42], consistent with the heteroepitaxial thin film being under residual compressive in-plane strain [30].

TABLE I. Model parameters of the steady-state DF spectra as shown in Fig. 5. See Eqs. (3a)–(3c) and the text for definitions. The broadening parameter $\gamma = 83$ meV.

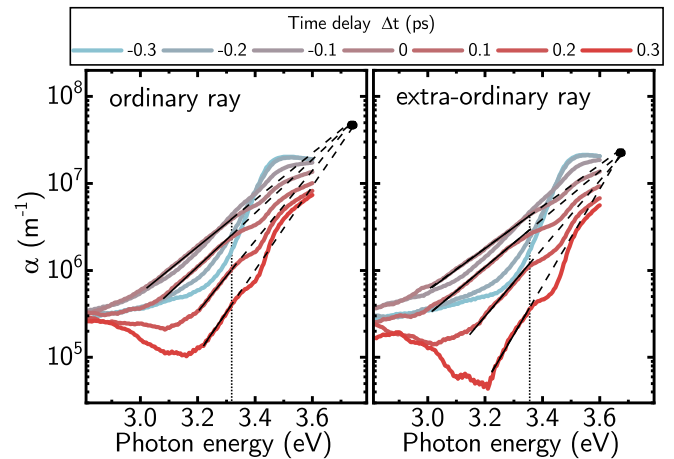| Parameter	ε_2^{sc}	ε_2^{pc}
A_X (eV^3)	1.97	2.11
A_C (eV^2)	12.67	13.54
$E_X(n = 1)$ (eV)	3.38	3.41
F_{EPC}	0.19	0.19

FIG. 6. Transient absorption coefficient corresponding to the ordinary and the extraordinary [38] ray for $\Delta t = -300$ fs (blue) to 300 fs (red) in steps of 100 fs. The vertical dotted lines indicate the position of the free-exciton energies in ZnO for polarization either parallel or perpendicular to the optic axis, which coincide with the high-energy limit of the exponential line shape of the absorption coefficient. The circles mark a crossing region of the slope lines, which is indicative of Urbach-rule absorption [43,52].

We obtain $F_{EPC} = 0.19$, which implies that the EPC contribution to our thin-film DF compared with discrete exciton contributions is rather weak [20,49]. The transient exciton energy E_X is depicted in Fig. 4(c). The range of time delays -100 fs $< \Delta t < 3$ ps is excluded from the line-shape analysis because the model parameters are uncertain for these Δt, where the absorption peak is not observed anymore in the measured spectral range. Instead, the peak position is simply read off from the maxima in the ε_2 spectra [Figs. 2(a) and 2(b)] to approximate the exciton energy, which is slightly lower than the true peak energy. The transient exciton energy E_X is increased by 80 meV at most after 3 ps and remains close to this value for another 3 ps. We conclude that in this case the increase in E_X due to band filling (Pauli blocking) and reduction in E_B^X dominate over the decrease in E_X due to band-gap renormalization [50]. The steady-state value of E_X is almost reached again after 20 ps, followed by a minimum observed for $\Delta t \approx 200$ ps similar to Ref. [3]. The minimum can be qualitatively explained by a maximum of the transient lattice temperature [1,51] leading to a decreased band-gap energy. After 5 ns, the transient exciton energy E_X is still about 10 meV lower than its steady-state value. Similarly, neither birefringence nor dichroism is fully restored yet. This observation can be a result of persistent carrier trapping [27]. However, we expect complete relaxation within 1 ms [51].

The absorption edge (Fig. 6) is smeared out upon optical excitation starting at $\Delta t = -100$ fs until about $\Delta t = 300$ fs and shows an exponential line shape whose slope lines intersect approximately at a single point. These observations indicate Urbach-rule absorption [43,52]. As originally reported by Urbach [53], the slope lines of the absorption coefficient cross at a common point for varying lattice temperature. However, the lattice temperature should not have changed much until $\Delta t = 300$ fs. Considering the intense

excitation of optical phonons (the hot-phonon effect [2]), it is also not clear whether the lattice temperature is a well-defined parameter in this nonequilibrium situation. See Appendix F for further discussion.

The physical origin of Urbach-rule absorption lies in the presence of microscopic (possibly stochastic) electric-field distributions, which are able to ionize the excitons [54]. Such electric fields can arise from defects in the crystal lattice, from disorder, or from a local lattice deformation [44,54,55]. Even if the MBE-grown ZnO thin film is subject to an anisotropic strain relaxation governed by interfacial dislocations [56], we suggest the exciton–LO-phonon interaction, which is paramount for the optical properties of polar semiconductors, to be responsible for the exponential line shape of the absorption coefficient: The charge carrier relaxation generates hot phonons that perturb the lattice potentials, which then act like disorder on the excitons. Furthermore, free excitons are still available exactly on the time scale of the appearance of Urbach-rule absorption $\Delta t = -100$ to 300 fs and become screened by the high carrier density later on [57]. Only weakly correlated electron-hole pairs (so-called Mahan excitons [58,59]) exist for high carrier density, which we assign to the peak structure in the DF after 1 ps [arrows in Figs. 2(a), 3(a), and 3(c)] as observed earlier [3].

The high-energy limit of the exponential absorption coefficient appears to coincide with the steady-state exciton energy ([60], vertical dotted lines in Fig. 6) without the blueshift due to the residual strain [42]. The spectral position of this feature does not change much (about 10 meV blueshift) [61]. The built-in electric field induced by the residual strain could be screened by the excited charge carriers. This observation hints again at the exciton–LO-phonon interaction as the decisive mechanism for the Urbach-rule absorption in this case [44].

Interestingly, the exciton energy seems to be stable on the time scale of the abovementioned Urbach-rule absorption (until $\Delta t = 300$ fs, Fig. 6) and increases only afterwards [Fig. 4(c)]. We speculate that this is related to the carrier density of states near the valence-band (VB) maximum and conduction-band (CB) minimum: These states become occupied only after thermalization among the carriers taking 200 fs (400 fs) for holes (electrons) [3]. Hence many-body effects modifying the transient exciton energy would set in only after carrier thermalization, i.e., establishment of a Fermi-Dirac distribution (further explanation below), which is in accordance with earlier investigations [62].

The photoexcited electron-hole pairs are expected to feature optical properties that can be described by the Drude model in the IR spectral range [50]. In Fig. 7 we compare the transient DF ε^{sc} (symbols) at $\Delta t = 200$ fs and the corresponding steady-state DF (dashed lines) to the simulated line shape of the sum of two Drude terms (solid lines) using the known carrier density and reasonable effective carrier masses [63,64] and mobilities. The transient data feature a reduction in ε_1^{sc} and a slight increase in ε_2^{sc}. The line shape of ε_1^{sc} resembles the Drude contributions for $\varepsilon_b = 4$ background dielectric constant, 50 cm^2/(V s) electron mobility and 3×10^{20} cm^{-3} carrier density. Still, the same line shape can also result from the low-energy absorption combined with the reduction in the background dielectric constant $\varepsilon_1 = \varepsilon_b$ induced by Kramers-Kronig relations [65] due to the absorption bleaching at the
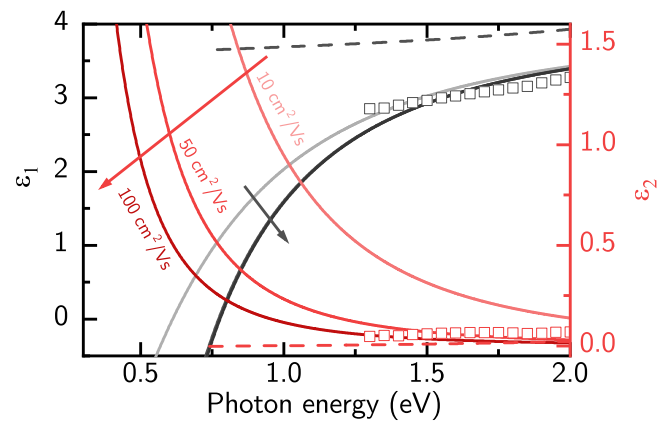

FIG. 7. Comparison of experimental data ε_2^{sc} (symbols) at $\Delta t = 200$ fs and the corresponding steady-state DF (dashed lines) to the simulated line shape of the sum of two Drude terms resulting from the electron-hole plasma [50]. The Drude model parameters are 3×10^{20} cm^{-3} charge carrier density, $\varepsilon_b = 4$ background dielectric constant, and 0.24 m_0 (0.59 m_0) effective electron (hole) masses [63,64] with m_0 electron rest mass. The electron mobilities are indicated in the plot, and hole mobilities are assumed to be lower by a factor of m_e/m_h. Note that the ε_1 curves for 50 and 100 cm^2/(Vs) electron mobility coincide within the line thickness in the plotted spectral range.

band gap. The line shape of ε_2^{sc} reveals no conclusive information here because our measured spectral range does not extend far enough into the IR spectral range to overlap with the strong curvature of the Drude term. Therefore we cannot rule out one or the other mechanism.

VI. CONCLUSION

In the experiment, the UV-pump laser (266 nm and 4.67 eV) promotes electrons from the light-hole, heavy-hole, and split-off VB to the CB in the vicinity of the Γ point and transfers excess energy to electrons and holes (Fig. 1). The optical excitation conditions are identical to Ref. [3]. Thus we expect similar carrier and phonon dynamics: Initially, the carrier distribution in momentum space follows the spectral distribution of the pump laser; that is, it features a peak and is nonthermal. A Fermi-Dirac distribution is reached within a few hundred femtoseconds. The process is called thermalization, and the state is typically referred to as "hot carriers." Thermalization is provided by carrier-carrier scattering and carrier-phonon scattering [1,2,51]. The thermalized carrier distributions are very broad because the large excess energy leads to carrier temperatures of a few thousand kelvins [66]. Multiple effects result from the presence of these hot carriers: (1) The VB maximum and CB minimum are occupied leading to partial Pauli blocking of band-to-band and excitonic transitions (band filling) [24,27,57]. Additional suppression of the excitonic absorption is expected from the screening by free charge carriers [67]. Hence absorption bleaching (decrease in ε_2) is observed at the band gap. Kramers-Kronig relations [65] enforce a simultaneous reduction in ε_1 in the nearby spectral range. (2) Holes scatter along the flat VB to the edge of the Brillouin zone, thereby dynamically promoting

new electronic transitions between valence bands [68] and prohibiting higher-energetic transitions, e.g., the E1 transition at 9 eV [69], which is, however, outside our measured spectral range. (3) Exchange and correlation interaction between the carriers leads to band-gap renormalization [50,57,70,71]. See Ref. [3] for a more thorough discussion of these effects.

The hot-carrier effects are captured by our first-principles calculations [59] for 10^{20} cm^{-3} electron-hole pairs in ideal bulk ZnO where confinement effects are neglected (Fig. 2). First-principles dichroism spectra [Fig. 2(d)] agree qualitatively with our measurements. Differences result from neglecting EPC and carrier confinement in the ideal bulk-ZnO model. The calculated birefringence features an offset already in the steady state which is related to the limited spectral range (up to 10 eV) for the Kramers-Kronig integral for ε_1.

Dichroism in the spectral range of the low-energy absorption could be expected, because various possible optical transitions in the Brillouin zone are subject to selection rules [72]. Yet, dichroism is small for all Δt in this spectral range, but the difference of the integrated spectra of ε_2 seems larger. Here, $\varepsilon_2^{\mathrm{sc}} > \varepsilon_2^{\mathrm{pc}}$ during the first picosecond after excitation. Both observations can be explained by inter-valence-band transitions near the A point (Fig. 1), where the energy difference between the topmost valence bands amounts to about 2.1 eV. Those inter-valence-band transitions are symmetry suppressed by optical selection rules [72] for light polarization parallel to the optic axes ($\varepsilon_2^{\mathrm{pc}}$). The presence of this weak dichroism hints at inter-valence-band transitions, but defect-related transitions cannot be totally excluded. This, in turn, diminishes the importance of the Drude term on the low-energy side of our measured spectral range.

The main differences compared with the observations for a polar *c*-plane-oriented ZnO thin film [3] are related to the remaining strain induced by the substrate and the missing surface band bending of the nonpolar *m*-plane surface [73,74]. Less excitonic enhancement at the absorption edge is expected on a nonpolar surface [42] while the phonon-dispersion relation seems to be resilient to polarity changes [74].

VII. SUMMARY

In summary, we have shown that time-resolved spectroscopic ellipsometry is an excellent tool to study pump-laser-induced transient optical anisotropy and enables distinction between birefringent and dichroic effects. The transient DF tensor in the spectral range 1.4–3.6 eV of an *m*-plane-oriented ZnO thin film after nonresonant UV excitation was obtained, and transient physical parameters were deduced from a line-shape analysis. Pump-induced switching from positive to negative birefringence was observed in the entire measured spectral range for 1 ps. Weak dichroism in the spectral range below 3.0 eV hints at contributions of inter-valence-band transitions, while the exponential line shape of the absorption coefficient just below the absorption edge can be related to Urbach absorption caused by exciton–LO-phonon interaction. Finally, the transient exciton energy corresponding to the three upper valence bands was increased by at most 80 meV after 3 ps.

APPENDIX A: NOISE REDUCTION AND ELLIPSOMETRIC DATA GENERATION

The experimental setup and the data reduction as well as error estimation are described in Refs. [3,28]. Additional steps of the data treatment are described in this Appendix. The experimental spectra are subject to noise due to intensity fluctuations of the driving Ti:sapphire laser and the nonlinear nature of the probe-white-light generation process. In order to reduce noise, we employ the combined interpolation, scale-change, and noise-reduction filter proposed by Le *et al.* [29]. The filter is based on a Gaussian kernel and trapezoidal-rule integration. In the same process, the spectra are interpolated from an unevenly spaced wavelength scale determined by the dispersion of the prism spectrometer to an *equidistant energy scale* [75]. This is generally desirable for the spectral analysis of the resulting dielectric function. Exemplary filtered reflectance-difference spectra are shown in the Supplemental Material. Note the fluctuations around 1.55 eV (800 nm) which result from diffraction effects the physical edge of a laser filter. Linear interpolations of the final ellipsometric parameters N, C, and S, which are much smoother than the reflectance-difference spectra, are used to generate the parameters around 1.55 eV.

The probe white light is chirped, i.e., photons with higher energy are delayed with respect to lower-energy photons, which results from the dispersion of the refractive index of
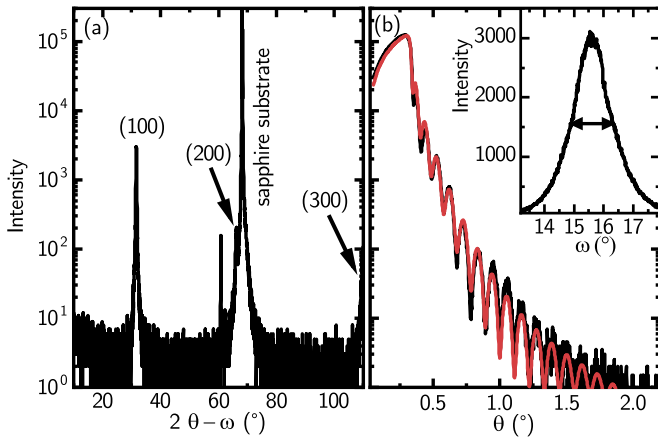
FIG. 8. (a) 2θ-ω x-ray diffraction scan of the main sample. (b) X-ray (Cu K-α anode) reflectivity along with a model fit of a reference *m*-ZnO thin film on an *m*-sapphire substrate which was grown under nominally identical conditions to those of the main sample. The inset in (b) shows the rocking curve of the (100) ZnO peak.

the CaF_2 crystal used for white-light generation and the glass support of the wire-grid polarizer ahead of the sample. As a consequence, the zero time delay $\Delta t = 0$ is not the same for every probe photon energy. The zero time delay is in principle arbitrary and was set during data acquisition to the position of the largest reflectance-difference signal. Therefore we readjust the energy–time-delay grid for the chirp, which is modeled with an even polynomial. Exemplary plots of the chirp-corrected data are provided in the Supplemental Material.

APPENDIX B: SAMPLE CHARACTERIZATION

The ZnO thin film was grown by molecular beam epitaxy (MBE) on an *m*-plane-oriented sapphire substrate similar to Ref. [30]. The *c* axis of ZnO is oriented perpendicular to the *c* axis of sapphire in this case. In Fig. 8(a), 2θ-ω x-ray diffraction scans demonstrate the sole (100) orientation [corresponding to $(10\bar{1}0)$ orientation in (*hkil*) notation] of the ZnO film with no sign of parasitic orientations. X-ray reflectivity data of a reference *m*-ZnO thin film grown on an *m*-sapphire substrate under identical conditions to those of the main sample are shown in Fig. 8(b). A layer stack model yields a film thickness of 37 nm and 2-nm roughness. The smooth surface has been confirmed by atomic force microscopy (AFM) measurements as displayed in Fig. 9 which indicate a root-mean-square roughness of about 1 nm. The rocking curve of the heteroepitaxial ZnO thin film shows a FWHM of about 1.5° [Fig. 2(b) inset], which is relatively narrow for such a thin film. Furthermore, the grain size along the growth direction, as extracted from the x-ray scans using the Scherrer formula, is limited by the film thickness confirming the overall high structural quality.

APPENDIX C: FIRST-PRINCIPLES CALCULATIONS

The first-principles calculations are based on many-body perturbation theory in order to investigate the optical properties of ZnO subject to electron-hole interactions. We use
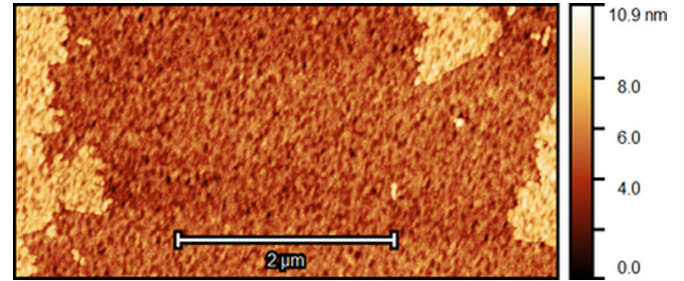

FIG. 9. The AFM image of the main sample reveals a smooth surface with about 1 nm roughness.

density functional theory (DFT) [76,77] to calculate Kohn-Sham states and energies and employ these to solve the Bethe-Salpeter equation (BSE) for the optical polarization function [78]. All DFT calculations are carried out using the Vienna *ab initio* simulation package [79–81] and the computational parameters given in Refs. [59,82]. The BSE calculation employs the implementation detailed in Refs. [83,84]. More details on the calculations are presented in Ref. [3]. The first-principles calculations constitute an ideal bulk-ZnO DF in contrast to the thin film measured here. The energy of the absorption edge is lower (no strain effect) and features a higher amplitude (ideal crystal structure).

APPENDIX D: KRAMERS-KRONIG CONSISTENCY

Kramers-Kronig relations (KKR) connect the line shape of the real and imaginary part of the DF. In order to check KKR consistency of a given DF, one can fit a KKR-consistent B-spline representation [85] to it. In our experiment, the relative difference between the wavelength-by-wavelength DF and the B-spline DF is at most 3%, which means that the wavelength-by-wavelength DF is approximately KKR-consistent. The wavelength-by-wavelength description was preferred over the B-spline representation in order to avoid any artificial oscillations [86,87] at the high-energy side of the spectrum for the subsequent line-shape analysis.

APPENDIX E: COMPLEX-PLANE REPRESENTATION OF THE DIELECTRIC FUNCTION

Complex-valued functions can be represented in the plane spanned by its real and imaginary part, which is called an Argand diagram [88]. This representation is termed a "Cole-Cole plot" when the dielectric function (DF) $\varepsilon = \varepsilon_1 + i\varepsilon_2$ is plotted in the ε_1-ε_2 plane [89]. The resulting line shows characteristic counterclockwise curves corresponding to resonances in the spectrum which are determined by the Kramers-Kronig relations [90]. This complex-plane representation is rarely reported [91,92] although it provides a beautiful way to emphasize the DF changes in resonances. The DF tensor components for the same time delays and spectral range as in Fig. 2 in complex-plane representation are shown in Fig. 3. Photon energy increases counterclockwise along the curve. Low-energy absorption is depicted near $\varepsilon_2 = 0$, while absorption bleaching is clearly seen by the shrinking radius of the semicircle.
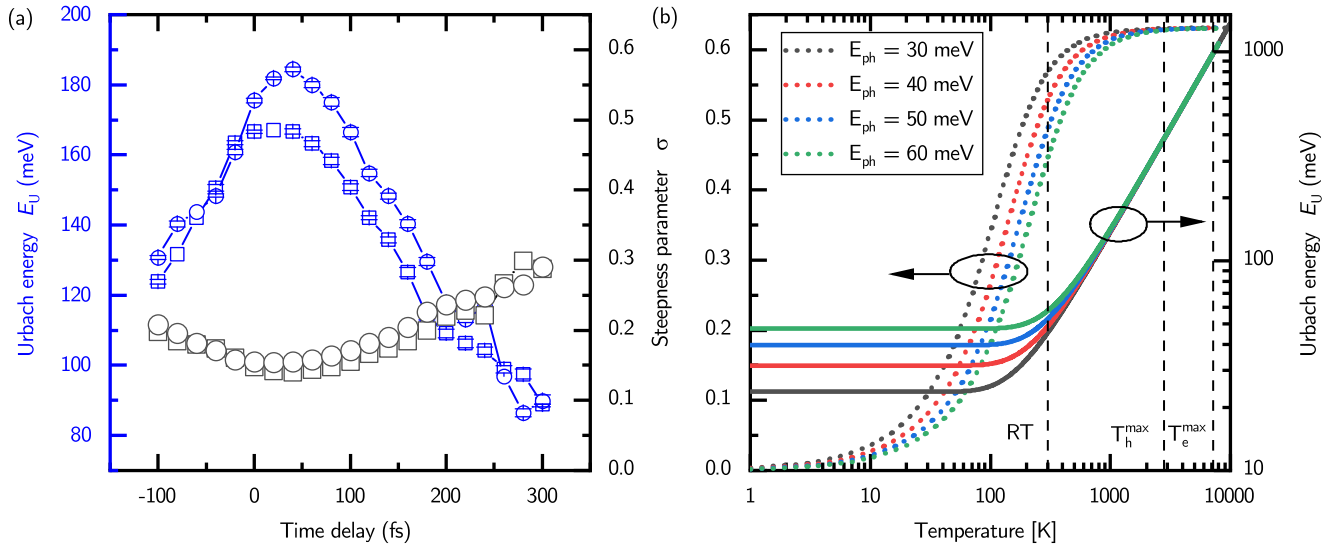
FIG. 10. (a) Transient Urbach energy E_U and steepness parameter σ as defined in Ref. [52] for exponential model fits (not shown) of the absorption coefficient. Squares correspond to the absorption coefficient of the ordinary ray, and circles correspond to the extraordinary ray. We assume 300 K lattice temperature and $E_{ph} = 50$ meV effective phonon energy in accordance with the literature [3,20,49]. (b) Theoretical steepness parameter σ and Urbach energy E_U for varying lattice temperature and E_{ph} as calculated from Eqs. (1) and (2) in Ref. [52]. Dashed lines indicate room temperature (RT) and the maximal electron (hole) temperature T_e (T_h) in the present experiment.

APPENDIX F: URBACH RULE ANALYSIS

An exponential line shape of the absorption coefficient [53] below the band gap can indicate the presence of Urbach-rule absorption [43,52]. It was demonstrated that the absorption coefficient of the ordinary ray and the extraordinary ray for $\Delta t = -100$ to 300 fs shows such an exponential line shape and that the corresponding slope lines cross each other approximately at the same point. The appearance of a "focal point" for varying lattice temperature is another criterion for Urbach-rule absorption [43]. In contrast to the original definition of the Urbach rule, we do not expect a change in lattice temperature on this time scale. Only the effective carrier temperatures are increasing in the sense that carriers gain excess energy. Note, however, that quasi-thermal equilibrium, which allows the definition of a temperature, might not be reached yet [3].

The transient Urbach energy $E_U = kT/\sigma$ [Fig. 10(a)] as defined in Ref. [52] and obtained from a model fit of the absorption coefficient (Fig. 6) increases to $E_U \approx 190$ meV at

most. In our case, it is a measure of the spectral range in which the absorption coefficient shows an exponential line shape. The increase in E_U is slightly larger for the fits corresponding to the extraordinary ray. The corresponding steepness parameter σ decreases from 0.2 to 0.15 assuming 300 K lattice temperature and $E_{ph} = 50$ meV effective phonon energy in accordance with the literature [3,20,49]. A decrease in σ can be related to increased exciton–LO-phonon interaction strength [44,93]. However, it is not clear whether it is valid to assume constant temperature and effective phonon energy or whether the lattice temperature is the correct parameter in this nonequilibrium system. An increase in T could overcompensate for an increase in E_U (as in our analysis) and thus could easily lead to an increase in σ. Theoretical curves of σ and E_U for varying lattice temperature are shown in Fig. 10(b). It is seen that the actual value of the effective phonon energy E_{ph} has a weak influence. This could indicate that the transient temperature parameter T is more relevant for the Urbach analysis of our experiment.

[1] A. Othonos, Probing ultrafast carrier and phonon dynamics in semiconductors, J. Appl. Phys. (Melville, NY) **83**, 1789 (1998).

[2] J. Shah, *Ultrafast Spectroscopy of Semiconductors and Semiconductor Nanostructures*, 2nd enlarged ed., Springer Series in Solid-State Sciences Vol. 115 (Springer, Berlin, 1999).

[3] S. Richter, O. Herrfurth, S. Espinoza, M. Rebarz, M. Kloz, J. A. Leveillee, A. Schleife, S. Zollner, M. Grundmann, J. Andreasson, and R. Schmidt-Grund, Ultrafast dynamics of hot charge carriers in an oxide semiconductor probed by femtosecond spectroscopic ellipsometry, New J. Phys. **22**, 083066 (2020).

[4] S. Espinoza, S. Richter, M. Rebarz, O. Herrfurth, R. Schmidt-Grund, J. Andreasson, and S. Zollner, Transient dielectric

functions of Ge, Si, and InP from femtosecond pump-probe ellipsometry, Appl. Phys. Lett. **115**, 052105 (2019).

[5] H. Fujiwara, *Spectroscopic Ellipsometry: Principles and Applications* (Wiley, Hoboken, NJ, 2007).

[6] M. Born, E. Wolf, and A. B. Bhatia, *Principles of Optics: Electromagnetic Theory of Propagation, Interference and Diffraction of Light*, 7th ed. (Cambridge University Press, Cambridge, 2016) .

[7] L. Mangot, G. Taupier, M. Romeo, A. Boeglin, O. Cregut, and K. D. Dorkenoo, Broadband transient dichroism spectroscopy in chiral molecules, Opt. Lett. **35**, 381 (2010).

[8] A. Trifonov, I. Buchvarov, A. Lohr, F. Würthner, and T. Fiebig, Broadband femtosecond circular dichroism spectrometer with

white-light polarization control, Rev. Sci. Instrum. **81**, 043104 (2010).

[9] J. Meyer-Ilse, D. Akimov, and B. Dietzek, Recent advances in ultrafast time-resolved chirality measurements: Perspective and outlook, Laser Photonics Rev. **7**, 495 (2013).

[10] K. Hiramatsu and T. Nagata, Communication: Broadband and ultrasensitive femtosecond time-resolved circular dichroism spectroscopy, J. Chem. Phys. **143**, 121102 (2015).

[11] V. Stadnytskyi, G. S. Orf, R. E. Blankenship, and S. Savikhin, Near shot-noise limited time-resolved circular dichroism pump-probe spectrometer, Rev. Sci. Instrum. **89**, 033104 (2018).

[12] M. Oppermann, B. Bauer, T. Rossi, F. Zinna, J. Helbing, J. Lacour, and M. Chergui, Ultrafast broadband circular dichroism in the deep ultraviolet, Optica **6**, 56 (2019).

[13] F. Auvray, D. Dennetiere, A. Giuliani, F. Jamme, F. Wien, B. Nay, S. Zirah, F. Polack, C. Menneglier, B. Lagarde, J. D. Hirst, and M. Réfrégiers, Time resolved transient circular dichroism spectroscopy using synchrotron natural polarization, Struct. Dyn. **6**, 054307 (2019).

[14] A. Mokhtari and J. Chesnoy, Resonant impulsive stimulated Raman scattering, Europhys. Lett. **5**, 523 (1988).

[15] J. Chesnoy and A. Mokhtari, Resonant impulsive-stimulated Raman scattering on malachite green, Phys. Rev. A **38**, 3566 (1988).

[16] F. Boschini, H. Hedayat, C. Piovera, C. Dallera, A. Gupta, and E. Carpene, A flexible experimental setup for femtosecond time-resolved broad-band ellipsometry and magneto-optics, Rev. Sci. Instrum. **86**, 013909 (2015).

[17] C. F. Klingshirn, *Zinc Oxide: From Fundamental Properties towards Novel Applications*, Springer Series in Materials Science Vol. 120 (Springer, Heidelberg, 2010).

[18] M. Lorenz, M. S. Ramachandra Rao, T. Venkatesan, E. Fortunato, P. Barquinha, R. Branquinho, D. Salgueiro, R. Martins, E. Carlos, A. Liu, F. K. Shan, M. Grundmann, H. Boschker, J. Mukherjee, M. Priyadarshini, N. DasGupta, D. J. Rogers, F. H. Teherani, E. V. Sandana, P. Bove *et al.*, The 2016 oxide electronic materials and oxide interfaces roadmap, J. Phys. D: Appl. Phys. **49**, 433001 (2016).

[19] S. Shokhovets, G. Gobsch, and O. Ambacher, Conduction band parameters of ZnO, Superlattices Microstruct. **39**, 299 (2006).

[20] M. D. Neumann, C. Cobet, N. Esser, B. Laumer, T. A. Wassner, M. Eickhoff, M. Feneberg, and R. Goldhahn, Optical properties of MgZnO alloys: Excitons and exciton-phonon complexes, J. Appl. Phys. (Melville, NY) **110**, 013520 (2011).

[21] K. Bohnert, G. Schmieder, and C. Klingshirn, Gain and reflection spectroscopy and the present understanding of the electron–hole plasma in II–VI compounds, Phys. Status Solidi B **98**, 175 (1980).

[22] C. J. Cook, S. Khan, G. D. Sanders, X. Wang, D. H. Reitze, Y. D. Jho, Y.-W. Heo, J.-M. Erie, D. P. Norton, and C. J. Stanton, Ultrafast carrier relaxation and diffusion dynamics in ZnO, in *Oxide-based Materials and Devices*, SPIE Proceedings, edited by F. H. Teherani, D. C. Look, C. W. Litton, and D. J. Rogers (SPIE, Bellingham, WA, 2010), p. 760304.

[23] M. A. M. Versteegh, T. Kuis, H. T. C. Stoof, and J. I. Dijkhuis, Ultrafast screening and carrier dynamics in ZnO: Theory and experiment, Phys. Rev. B **84**, 035207 (2011).

[24] P.-C. Ou, J.-H. Lin, and W.-F. Hsieh, Spectral dependence of transient reflectance in a ZnO epitaxial film at room temperature, Appl. Phys. B: Lasers Opt. **106**, 399 (2012).

[25] A. Yamamoto, T. Kido, T. Goto, Y. Chen, T. Yao, and A. Kasuya, Dynamics of photoexcited carriers in ZnO epitaxial thin films, Appl. Phys. Lett. **75**, 469 (1999).

[26] S. Acharya, S. Chouthe, H. Graener, T. Böntgen, C. Sturm, R. Schmidt-Grund, M. Grundmann, and G. Seifert, Ultrafast dynamics of the dielectric functions of ZnO and BaTiO$_3$ thin films after intense femtosecond laser excitation, J. Appl. Phys. (Melville, NY) **115**, 053508 (2014).

[27] L. Foglia, S. Vempati, B. Tanda Bonkano, L. Gierster, M. Wolf, S. Sadofev, and J. Stähler, Revealing the competing contributions of charge carriers, excitons, and defects to the non-equilibrium optical properties of ZnO, Struct. Dyn. **6**, 034501 (2019).

[28] S. Richter, M. Rebarz, O. Herrfurth, S. Espinoza, R. Schmidt-Grund, and J. Andreasson, Broadband femtosecond spectroscopic ellipsometry, Rev. Sci. Instrum. **92**, 033104 (2021).

[29] V. L. Le, T. J. Kim, Y. D. Kim, and D. E. Aspnes, Combined interpolation, scale change, and noise reduction in spectral analysis, J. Vac. Sci. Technol., B **37**, 052903 (2019).

[30] J.-M. Chauveau, P. Vennéguès, M. Laügt, C. Deparis, J. Zúñiga-Pérez, and C. Morhain, Interface structure and anisotropic strain relaxation of nonpolar wurtzite (1120) and (1010) orientations: ZnO epilayers grown on sapphire, J. Appl. Phys. (Melville, NY) **104**, 073535 (2008).

[31] The penetration depth was calculated from the reference DF that was obtained by spectroscopic ellipsometry measurements with a dual-rotating-compensator ellipsometer (J.A. Woollam RC2, 193–1700 nm spectral range).

[32] H. G. Tompkins and E. A. Irene, *Handbook of Ellipsometry* (Andrew, Norwich, NY, 2005).

[33] J. Hermann, M. Benfarah, S. Bruneau, E. Axente, G. Coustillier, T. Itina, J.-F. Guillemoles, and P. Alloncle, Comparative investigation of solar cell thin film processing using nanosecond and femtosecond lasers, J. Phys. D: Appl. Phys. **39**, 453 (2006).

[34] S. Zoppel, H. Huber, and G. A. Reider, Selective ablation of thin Mo and TCO films with femtosecond laser pulses for structuring thin film solar cells, Appl. Phys. A: Mater. Sci. Process. **89**, 161 (2007).

[35] G. Heise, M. Dickmann, M. Domke, A. Heiss, T. Kuznicki, J. Palm, I. Richter, H. Vogt, and H. P. Huber, Investigation of the ablation of zinc oxide thin films on copper–indium-selenide layers by ps laser pulses, Appl. Phys. A: Mater. Sci. Process. **104**, 387 (2011).

[36] M. Schubert, Polarization-dependent optical parameters of arbitrarily anisotropic homogeneous layered systems, Phys. Rev. B **53**, 4265 (1996).

[37] D. A. G. Bruggeman, Berechnung verschiedener physikalischer Konstanten von heterogenen Substanzen. I. Dielektrizitätskonstanten und Leitfähigkeiten der Mischkörper aus isotropen Substanzen, Ann. Phys. (Berlin) **416**, 636 (1935).

[38] Indices "o" and "e" refer to the propagation constants of the ordinary and extraordinary ray, respectively. Here, the extraordinary ray shall be polarized entirely parallel to the material's optic axis as it occurs for propagation perpendicular it.

[39] M. Bass, *Geometrical and Physical Optics, Polarized Light, Components and Intruments*, 3rd ed., Handbook of Optics Vol. 1 (McGraw-Hill, New York, 2010) .

[40] See Supplemental Material at http://link.aps.org/supplemental/10.1103/PhysRevResearch.3.013246 for additional plots of the

data reduction, first-principles calculations, the transient dielectric function, and the absorption coefficient. See also Ref. [28] for more experimental details.

[41] The time delay $\Delta t = 0$ can be defined arbitrarily and was set during data acquisition to the position of the first arising signal in the UV spectral range. During correction of the probe chirp, $\Delta t = 0$ was retroactively assigned to the position of the largest initial *change*. Its spectral dependence follows an even polynomial function to correct the energy–time-delay grid for the chirp of the probe laser pulse. See the Supplemental Material.

[42] M. Cobet, Ellipsometric study of ZnO from multimode formation of exciton-polaritons to the core-level regime, Ph.D. thesis, Technische Universität Berlin, 2010.

[43] M. V. Kurik, Urbach rule, Phys. Status Solidi A **8**, 9 (1971).

[44] H. Sumi and Y. Toyozawa, Urbach-Martienssen rule and exciton trapped momentarily by lattice vibrations, J. Phys. Soc. Jpn. **31**, 342 (1971).

[45] In Fig. 4(b), the offset of the integrated value of $\varepsilon_2^{\mathrm{sc}}$ with respect to the integrated value of $\varepsilon_2^{\mathrm{pc}}$ is related to the fact that the absorption sets in at lower photon energy for $\varepsilon_2^{\mathrm{sc}}$ (lower exciton energy) which is determined by optical selection rules [72].

[46] R. J. Elliott, Intensity of optical absorption by excitons, Phys. Rev. **108**, 1384 (1957).

[47] G. Rossbach, M. Feneberg, M. Röppischer, C. Werner, N. Esser, C. Cobet, T. Meisch, K. Thonke, A. Dadgar, J. Bläsing, A. Krost, and R. Goldhahn, Influence of exciton-phonon coupling and strain on the anisotropic optical response of wurtzite AlN around the band edge, Phys. Rev. B **83**, 195202 (2011).

[48] K. Oki and Y. Ishitani, Influence of LO and LA phonon processes on thermal-nonequilibrium excitation and deexcitation dynamics of excitons in GaN, AlN, and ZnO, J. Appl. Phys. (Melville, NY) **125**, 205705 (2019).

[49] S. Shokhovets, O. Ambacher, B. K. Meyer, and G. Gobsch, Anisotropy of the momentum matrix element, dichroism, and conduction-band dispersion relation of wurtzite semiconductors, Phys. Rev. B **78**, 035207 (2008).

[50] C. F. Klingshirn, *Semiconductor Optics*, Advanced Texts in Physics (Springer, New York, 2005).

[51] S. K. Sundaram and E. Mazur, Inducing and probing nonthermal transitions in semiconductors using femtosecond laser pulses, Nat. Mater. **1**, 217 (2002).

[52] I. Studenyak, M. Kranjec, and M. Kurik, Urbach rule in solid state physics, Int. J. Opt. Appl. **4**, 76 (2014).

[53] F. Urbach, The long-wavelength edge of photographic sensitivity and of the electronic absorption of solids, Phys. Rev. **92**, 1324 (1953).

[54] J. D. Dow and D. Redfield, Toward a unified theory of Urbach's rule and exponential absorption edges, Phys. Rev. B **5**, 594 (1972).

[55] J. G. Liebler, S. Schmitt-Rink, and H. Haug, Theory of the absorption tail of Wannier excitons in polar semiconductors, J. Lumin. **34**, 1 (1985).

[56] This could lead to inhomogeneous strain gradients, especially along the [0001] direction.

[57] R. Zimmermann, Nonlinear optics and the Mott transition in semiconductors, Phys. Status Solidi B **146**, 371 (1988).

[58] G. D. Mahan, Excitons in degenerate semiconductors, Phys. Rev. **153**, 882 (1967).

[59] A. Schleife, C. Rödl, F. Fuchs, K. Hannewald, and F. Bechstedt, Optical Absorption in Degenerately Doped Semiconductors: Mott Transition or Mahan Excitons? Phys. Rev. Lett. **107**, 236405 (2011).

[60] M. Cobet, C. Cobet, M. R. Wagner, N. Esser, C. Thomsen, and A. Hoffmann, Polariton effects in the dielectric function of ZnO excitons obtained by ellipsometry, Appl. Phys. Lett. **96**, 031904 (2010).

[61] This observation could indicate the general stability of the exciton energy with increasing carrier density [50], which can be traced back to the charge neutrality of the exciton [57].

[62] H. Kalt and M. Rinker, Band-gap renormalization in semiconductors with multiple inequivalent valleys, Phys. Rev. B **45**, 1139 (1992).

[63] W. S. Baer, Faraday rotation in ZnO: Determination of the electron effective mass, Phys. Rev. **154**, 785 (1967).

[64] K. Hümmer, Interband magnetoreflection of ZnO, Phys. Status Solidi B **56**, 249 (1973).

[65] P. Y. Yu and M. Cardona, *Fundamentals of Semiconductors* (Springer, Berlin, 2010).

[66] J. Shah, Hot electrons and phonons under high intensity photoexcitation of semiconductors, Solid-State Electron. **21**, 43 (1978).

[67] H. Haug and S. W. Koch, *Quantum Theory of the Optical and Electronic Properties of Semiconductors*, 5th ed. (World Scientific, Hackensack, NJ, 2009).

[68] A. Segura, J. Bouvier, M. V. Andrés, F. J. Manjón, and V. Muñoz, Strong optical nonlinearities in gallium and indium selenides related to inter-valence-band transitions induced by light pulses, Phys. Rev. B **56**, 4075 (1997).

[69] M. D. Neumann, Einfluss der Elektron-Loch-Wechselwirkung auf die dielektrische Funktion von ZnO, MgO und hexagonalem MgZnO, Ph.D. thesis, Technische Universität Berlin, 2015.

[70] J. G. Gay, Screening of excitons in semiconductors, Phys. Rev. B **4**, 2567 (1971).

[71] C. Klingshirn and H. Haug, Optical properties of highly excited direct gap semiconductors, Phys. Rep. **70**, 315 (1981).

[72] R. C. Casella, Symmetry of wurtzite, Phys. Rev. **114**, 1514 (1959).

[73] T. Onuma, N. Sakai, T. Igaki, T. Yamaguchi, A. A. Yamaguchi, and T. Honda, Comparative study of surface recombination in hexagonal GaN and ZnO surfaces, J. Appl. Phys. (Melville, NY) **112**, 063509 (2012).

[74] J. Zúñiga-Pérez, V. Consonni, L. Lymperakis, X. Kong, A. Trampert, S. Fernández-Garrido, O. Brandt, H. Renevier, S. Keller, K. Hestroffer, M. R. Wagner, J. S. Reparaz, F. Akyol, S. Rajan, S. Rennesson, T. Palacios, and G. Feuillet, Polarity in GaN and ZnO: Theory, measurement, growth, and devices, Appl. Phys. Rev. **3**, 041303 (2016).

[75] A slight modification must be made to Eq. (21c) in Ref. [29]. In order to convert unevenly spaced wavelength scales, $\Delta \lambda$ must be kept inside the summation. We thank Prof. David Aspnes for pointing this out.

[76] P. Hohenberg and W. Kohn, Inhomogeneous electron gas, Phys. Rev. **136**, B864 (1964).

[77] W. Kohn and L. J. Sham, Self-consistent equations including exchange and correlation effects, Phys. Rev. **140**, A1133 (1965).

[78] G. Onida, L. Reining, and A. Rubio, Electronic excitations: Density-functional versus many-body Green's-function approaches, Rev. Mod. Phys. **74**, 601 (2002).

[79] G. Kresse and J. Furthmüller, Efficient iterative schemes for *ab initio* total-energy calculations using a plane-wave basis set, Phys. Rev. B **54**, 11169 (1996).

[80] G. Kresse and D. Joubert, From ultrasoft pseudopotentials to the projector augmented-wave method, Phys. Rev. B **59**, 1758 (1999).

[81] M. Gajdoš, K. Hummer, G. Kresse, J. Furthmüller, and F. Bechstedt, Linear optical properties in the projector-augmented wave methodology, Phys. Rev. B **73**, 045112 (2006).

[82] A. Schleife, C. Rödl, F. Fuchs, J. Furthmüller, and F. Bechstedt, Optical and energy-loss spectra of MgO, ZnO, and CdO from *ab initio* many-body calculations, Phys. Rev. B **80**, 035112 (2009).

[83] C. Rödl, F. Fuchs, J. Furthmüller, and F. Bechstedt, *Ab initio* theory of excitons and optical properties for spin-polarized systems: Application to antiferromagnetic MnO, Phys. Rev. B **77**, 184408 (2008).

[84] F. Fuchs, C. Rödl, A. Schleife, and F. Bechstedt, Efficient $\mathcal{O}(N^2)$ approach to solve the Bethe-Salpeter equation for excitonic bound states, Phys. Rev. B **78**, 085103 (2008).

[85] B. Johs and J. S. Hale, Dielectric function representation by B-splines, Phys. Status Solidi A **205**, 715 (2008).

[86] D. V. Likhachev, Selecting the right number of knots for B-spline parameterization of the dielectric functions in spectroscopic ellipsometry data analysis, Thin Solid Films **636**, 519 (2017).

[87] D. V. Likhachev, On the optimization of knot allocation for B-spline parameterization of the dielectric function in spectroscopic ellipsometry data analysis, J. Appl. Phys. (Melville, NY) **129**, 034903 (2021).

[88] E. T. Whittaker and G. N. Watson, *A Course of Modern Analysis* (Cambridge University Press, Cambridge, 2013).

[89] K. S. Cole and R. H. Cole, Dispersion and absorption in dielectrics I. Alternating current characteristics, J. Chem. Phys. **9**, 341 (1941).

[90] T. A. Witten and S. R. Nagel, Argand diagrams of dielectric response, Solid State Commun. **16**, 185 (1975).

[91] V. V. Harutunian, V. A. Gevorkian, and G. N. Eritsian, Parameters of interband transitions in corundum crystals, Phys. Status Solidi B **183**, K23 (1994).

[92] S. Cabuk and A. Mamedov, Argand diagram and oscillation description of electron state in ferroelastic crystals, Ferroelectrics **307**, 19 (2004).

[93] Y. Toyozawa, On the dynamical behavior of an exciton, Prog. Theor. Phys. Suppl. **12**, 111 (1959).